

Understanding Interfacial Alignment in Solution Coated Conjugated Polymer Thin Films

Ge Qu,[†] Xikang Zhao,[‡] Gregory M. Newbloom,[§] Fengjiao Zhang,[†] Erfan Mohammadi,[†] Joseph W. Strzalka,^{||} Lilo D. Pozzo,[§] Jianguo Mei,^{‡,†,ib} and Ying Diao^{*,†,ib}

[†]Department of Chemical and Biomolecular Engineering, University of Illinois Urbana–Champaign, 600 S. Mathews Avenue, Urbana, Illinois 61801, United States

[‡]Department of Chemistry, Purdue University, West Lafayette, Indiana 47907, United States

[§]Department of Chemical Engineering, University of Washington, Box 351750, Seattle, Washington 98195-1750, United States

^{||}X-ray Science Division, Argonne National Laboratory, Argonne, Illinois 60439, United States

Supporting Information

ABSTRACT: Domain alignment in conjugated polymer thin films can significantly enhance charge carrier mobility. However, the alignment mechanism during meniscus-guided solution coating remains unclear. Furthermore, interfacial alignment has been rarely studied despite its direct relevance and critical importance to charge transport. In this study, we uncover a significantly higher degree of alignment at the top interface of solution coated thin films, using a donor–acceptor conjugated polymer, poly(diketopyrrolopyrrole-*co*-thiophene-*co*-thieno[3,2-*b*]thiophene-*co*-thiophene) (DPP2T-TT), as the model system. At the molecular level, we observe in-plane π – π stacking anisotropy of up to 4.8 near the top interface with the polymer backbone aligned parallel to the coating direction. The bulk of the film is only weakly aligned with the backbone oriented transverse to coating. At the mesoscale, we observe a well-defined fibril-like morphology at the top interface with the fibril long axis pointing toward the coating direction. Significantly smaller fibrils with poor orientational order are found on the bottom interface, weakly aligned orthogonal to the fibrils on the top interface. The high degree of alignment at the top interface leads to a charge transport anisotropy of up to 5.4 compared to an anisotropy close to 1 on the bottom interface. We attribute the formation of distinct interfacial morphology to the skin-layer formation associated with high Peclet number, which promotes crystallization on the top interface while suppressing it in the bulk. We further infer that the interfacial fibril alignment is driven by the extensional flow on the top interface arisen from increasing solvent evaporation rate closer to the meniscus front.

KEYWORDS: interfacial, alignment, conjugated polymer, solution printing, morphology, polymer crystallization, charge transport

INTRODUCTION

Conjugated polymers (CPs) have been intensively studied in recent decades owing to their potential applications in a wide range of technologies from flexible electronics, alternative energy conversion devices, to biomedical imaging. A major advantage of conjugated polymers is their compatibility with low-cost, high-throughput manufacturing methods such as roll-to-roll printing. The solution printing process has a direct impact on the thin film morphology across multiple length scales. It is well-known that thin film morphology characteristics can modulate charge transport properties in conjugated polymers by orders of magnitude.¹ At molecular scale, the extent of order in the crystalline/aggregated domains is described by paracrystallinity. In thin films with isotropic domain orientations, paracrystallinity has been shown to limit global charge transport.² Besides the importance of paracrystallinity to interchain charge transport, backbone planarity was shown to be critical to intrachain charge transport, which explains the excellent performance of several

nearly amorphous high molecular weight polymers recently reported.^{3,4} At mesoscale, connectivity between crystalline/aggregated domains is of critical importance; intergrain “tie-chains” were proposed as charge-transport highways,^{5,6} while abrupt grain boundaries that interrupt backbone conjugation are detrimental to charge transport,^{7,8} the extent to which may depend on the grain boundary orientation. It was also demonstrated that domain alignment in polymer thin films can enhance charge transport from a few times to over an order of magnitude.^{9–14} However, there has not been a systematic study reported to elucidate the origin of this phenomenon with regard to charge transport mechanisms.

Driven by the large performance gain from domain alignment, many methods have been developed to induce alignment in

Received: June 7, 2017

Accepted: August 1, 2017

Published: August 1, 2017

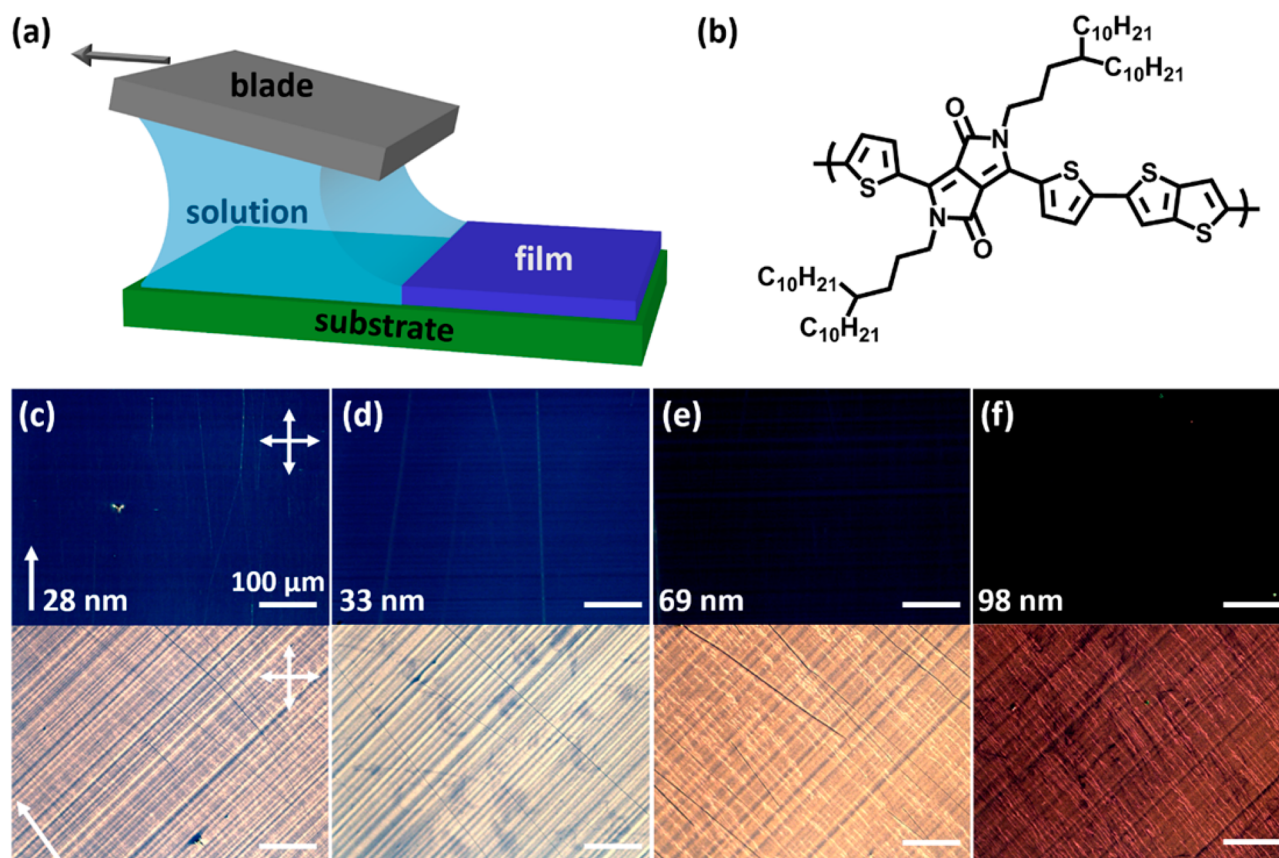


Figure 1. Solution coating of DPP2T-TT thin films and resulting birefringence for films of various thicknesses under cross-polarized microscopy. (a) Schematic of solution coating. (b) Molecular structure of DPP2T-TT. The film thicknesses are (c) 28 nm, (d) 33 nm, (e) 69 nm, and (f) 98 nm coated from solutions with concentrations of 5, 7, 10, 14 mg/mL, respectively. The first and the second rows of images correspond to films with coating direction oriented 0° and 45° with respect to the axis of the polarizer. The arrows at bottom left denote the coating direction, and the crossed arrows indicate orientations of the crossed polarizers. Scale bars are $100\ \mu\text{m}$ in all images.

conjugated polymer thin films, including mechanical rubbing,¹⁵ grooved template directed solution deposition,^{16,17} and unidirectional coating.^{11,13,14,18,19} Most unidirectional coating methods reported employed a liquid crystalline conjugated polymer to attain the high degree of alignment.^{11,13,18} On the other hand, depending on the specific system and the coating/printing conditions, the degree of alignment can vary from nearly isotropic (dichroic ratio ~ 1)²⁰ to highly aligned (dichroic ratio > 10).¹⁴ So far, the mechanism for attaining in-plane alignment during unidirectional coating/printing remains unclear. Here, we refer the in-plane alignment to the alignment of the polymer rod long axis parallel to the substrate plane and the out-of-plane alignment to the alignment of the polymer rod long axis with the substrate normal. Although most studies attribute the observed in-plane alignment to shear flow during coating, the shear rate is in fact along the out-of-plane direction, and is minimal in-plane. It is unclear to what extent and by what mechanism out-of-plane shear can induce in-plane alignment. In addition, contributions of other flow types are often ignored, such as extension and compression which are prominent in evaporation driven capillary flows that occur during solution coating/printing.

Although domain alignment has been extensively investigated, fewer studies distinguished alignment at the interface from that in the bulk of the thin film. On the other hand, interfacial morphology at the semiconductor–dielectric interface is directly relevant to charge transport in field-effect transistors. Morphologies at the interface distinct from that in the bulk have been

observed, including out-of-plane molecular orientation^{21–23} and in-plane backbone alignment.^{14,24} Regarding in-plane alignment, Schuettfort and McNeill et al. found a high degree of backbone alignment at the surface of zone-casted poly[2,5-bis(3-tetradecylthiophene-2-yl)thieno[3,2-*b*]thiophene] (PBTTT) films, compared to little alignment in the bulk of as-cast films.²⁴ Schott and Sirringhaus et al. observed a lower degree of alignment at the film surface compared to that in the bulk, in diketopyrrolopyrrole-benzotriazole copolymer (DPP-BTz) thin films coated using a soft blade.¹⁴ In addition, Patel and Kramer et al. observed different degrees of alignment at the top and bottom interfaces in blade-coated cyclopentadithiophen-thiadiazolopyridine copolymer (PCDTPT) thin films, a phenomenon dependent on the coating speed.²⁵ However, the underlying mechanism for a distinct interfacial morphology has yet to be elucidated.

In this work, we observed significantly different morphology at the free interface as compared to that in the bulk for solution coated poly(diketopyrrolopyrrole-*co*-thiophene-*co*-thieno[3,2-*b*]thiophene-*co*-thiophene) (DPP2T-TT) thin films. The air–film free interface exhibits fibril-like morphology; the polymer backbone extends parallel to the long axis of the fibrils, both of which aligned along the coating direction under most conditions tested. Interestingly, moving from the free interface to the bulk, the polymer backbone and the fibril long axis both alter in in-plane orientation to be either weakly aligned transverse to the coating direction or nearly isotropic, depending on the thickness

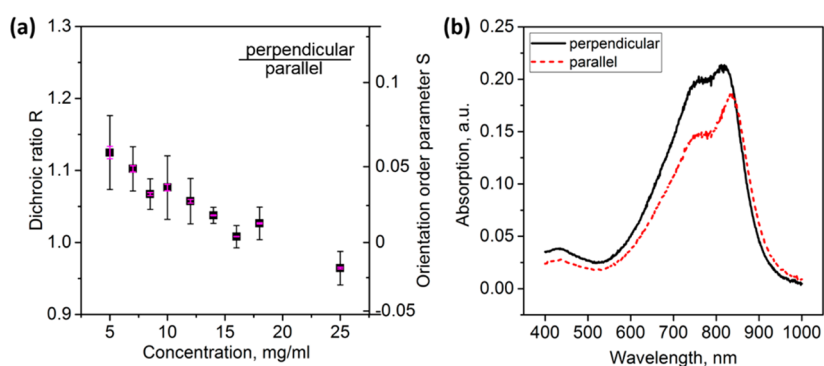


Figure 2. Degree of alignment in the bulk of coated thin films characterized using polarized UV–vis spectroscopy. (a) Dichroic ratio R and in-plane orientation order parameter S from polarized UV–vis spectroscopy as a function of film concentration/thickness. R and S were calculated from the peak absorbance at approximately 820 nm. The error bars of the same color correspond to the standard deviation of R , and those with a different color correspond to S . Error bars were obtained from 3 measurements of independent samples. (b) Polarized UV–vis absorption spectra in parallel and perpendicular orientations for films coated from 5 mg/mL solution. For both images, parallel and perpendicular orientations are defined in terms of the coating direction with respect to the axis of the polarizer.

of the film. Higher degrees of alignment at the free interface give rise to high charge transport anisotropy of up to ~ 6 , with favored charge transport direction along the polymer backbone. This is in contrast to a low charge transport anisotropy of ~ 1 obtained at the buried interface, whose morphology resembles that of the bulk. We further show that the preferred charge transport direction is strongly correlated with the preferred in-plane orientation of the polymer backbone. Finally, we propose a mechanism based on skin-layer formation and extensional flow induced in-plane alignment, in contrast to what has been widely hypothesized that shear flow drives alignment during meniscus-guided coating.

RESULTS

To characterize molecular alignment in solution coated thin films, we prepared DPP2T-TT films using a meniscus guided coating method wherein the ink solution was sandwiched between a moving blade and a substrate (Figure 1a). The method is detailed in previous publications,^{26,27} originated from evaporative assembly known as the “coffee ring effect”.²⁸ Briefly, DPP2T-TT (Figure 1b) thin films were coated from chloroform solutions at various concentrations (3 mg/mL to 25 mg/mL) on octadecyltrichlorosilane (ODTS) treated 300 nm SiO₂ on Si(100) substrates. The ODTS surface treatment was applied to minimize charge traps at the semiconductor–dielectric interface. The coating speed was 0.5 mm/s, and the substrate temperature was controlled at 25 °C. By changing the solution concentration, the film thickness was varied from 20.8 ± 0.8 nm (3 mg/mL) to 168 ± 7 nm (25 mg/mL) to systematically vary the fraction of the interfacial layer out of the bulk (Figure S1). The coating speed of 0.5 mm/s falls within the evaporation regime of solution coating (Figure S2). We further show that varying solution concentration did not alter the polymer aggregation state (Figures S4, S5, Table S1).

We next employed a suite of techniques probing the interfacial and bulk morphology across multiple length scales. We performed cross-polarized optical microscopy (CPOM) for visualizing global alignment and crystallinity, polarized UV–vis spectroscopy for quantifying polymer backbone alignment in the bulk of the film, grazing incidence wide-angle X-ray scattering (GIWAXS) for probing bulk and interfacial alignment in crystalline domains, and atomic force microscopy (AFM) for

characterizing mesoscale morphology at the free and buried interfaces.

Characterization of Bulk Alignment. First, we applied cross-polarized optical microscopy (CPOM) whereby the observed birefringence offers a qualitative characterization of the degree of in-plane alignment within the crystalline domains. For films exhibiting global alignment, an extinction of light is expected when the long axis of the polymer backbone in the crystallites is aligned with one of the polarizers. We observed light extinction in solution coated thin films when the coating direction was at 0° and 90° with respect to the axis of the polarizer (Figure 1c–f), indicating that the polymer backbone in crystalline domains is aligned along or transverse to the coating direction. This inference is consistent with the observation that the brightest reflection occurred when the coating direction was oriented 45° with respect to the polarizer. With increasing concentration/film thickness, an increasing and then decreasing trend in birefringence was observed (Figure S3). Although birefringence is correlated with the degree of alignment in the film, it is also proportional to the film thickness and the degree of crystallinity. The initial increase in birefringence (Figure 1c,d) may be attributed to enhanced polymer alignment and/or increase in film thickness. However, the decrease of birefringence at higher concentrations (Figure 1e,f) indicates a lower degree of alignment and/or crystallinity in thicker films. To quantify the degree of alignment in the bulk of the film, we further employed polarized UV–vis spectroscopy.

Polarized UV–vis spectroscopy measurements were performed on DPP2T-TT thin films coated on ODTS treated glass slides with the light polarization direction oriented either parallel or perpendicular to the coating direction. Because the transition dipole is principally along the polymer backbone direction,^{29–31} the UV–vis absorbance is expected to be the highest when the backbone is aligned with the polarization direction of the UV light. The degree of alignment of the polymer backbone can be characterized in terms of the dichroic ratio $R = A_{\text{perp}}/A_{\text{para}}$ with A_{perp} and A_{para} denoting the absorbance when the coating direction is perpendicular and parallel to the electric field pass direction of the polarizer. We note that R only provides a lower bound to the degree of backbone alignment, as the transition dipole may have a nonzero component normal to the polymer backbone.^{29,32} We calculated R values using the peak absorbance at 820 nm (Figure 2a), as the shoulder at 760 nm may not be

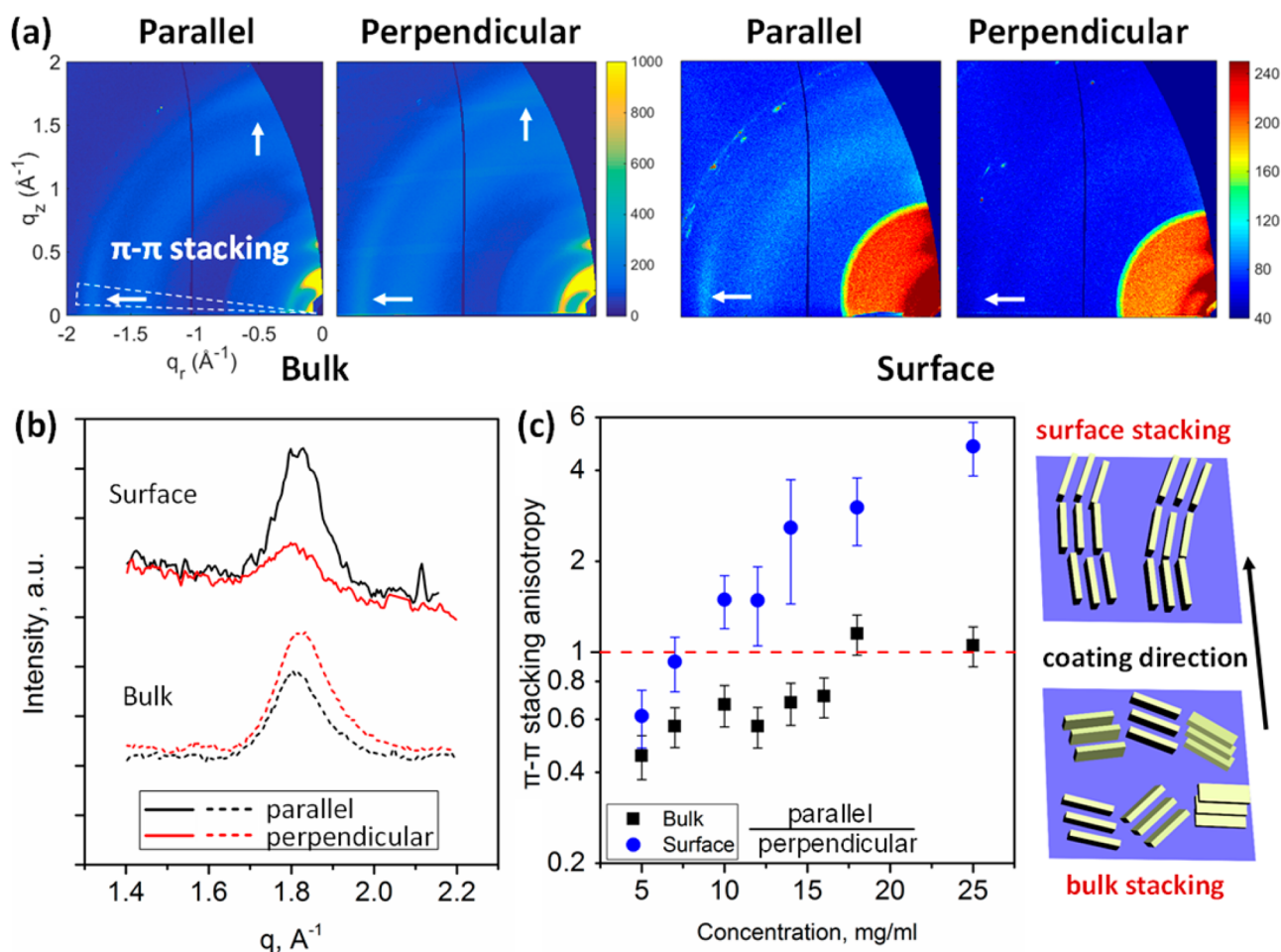


Figure 3. Surface vs bulk morphology and alignment probed by GIWAXS. (a) GIWAXS patterns for the 14 mg/mL (98 ± 2 nm) DPP2T-TT thin film, measured in parallel and perpendicular orientations with 0.2° incident angle for bulk measurement and 0.08° incident angle for surface measurement. (b) Comparison of the in-plane orientation of the film surface and the bulk film. Path length corrected intensity of the (010) π - π stacking peaks indicates the preferred in-plane orientation of the π - π stacks, obtained from a sector cut on the GIXD images with $-88^\circ < \chi < -83^\circ$ (cut area indicated in (a)). Surface peaks were scaled by a factor of 5 for direct comparison with the bulk case. (c) In-plane alignment indicated from the π - π stacking anisotropy P of the edge-on π - π stacking peak in the bulk and at the film surface. Error bars were obtained from peak intensity error resulting from incident angle alignment as well as from error of peak fitting. The schematics show the alignment of the π -stack at the film surface vs the bulk.

uniquely assigned to a single vibrational peak.³² We further calculated the orientational order parameter $S = (R - 1)/(R + 1)$ to represent the degree of backbone alignment on a scale from -1 to 1 , with 0 denoting completely isotropic, 1 uniaxially aligned perpendicular to the coating direction, and -1 uniaxially aligned parallel to coating.³³ Calculation of S from R as shown above is based on the assumption that the UV-vis absorbance scales with the magnitude of transition dipole moments projected along the polarization direction of light, following $A_{\text{para}} \propto \langle \cos^2 \phi \rangle$, wherein ϕ is the angle between the transition dipole and the light polarization direction.³⁴ With $R > 1$ and $S > 0$ at most conditions, we infer that the polymer backbone was preferentially oriented perpendicular to the coating direction in the bulk of the thin film. However, the degree of alignment is at best weak and at worst isotropic. Even the thinnest film (~ 28 nm) coated from 5 mg/mL solution exhibited a dichroic ratio R (820 nm) of only 1.12, corresponding to $S = 0.06$. We further observed a decreasing trend of dichroic ratio with increasing concentration/film thickness, which is consistent with decreasing birefringence observed from CPOM (Figure 1), assuming that the initial increase in birefringence was due to increase in film thickness.

Characterization of Interfacial Morphology. We next performed GIWAXS and AFM to probe surface (film-air interface) morphology as compared to the bulk and the buried interface (film-substrate interface). While UV-vis spectroscopy probes both the crystalline and the amorphous domains, GIWAXS signals come from the crystalline domains only. To evaluate the anisotropy of the in-plane molecular packing, GIWAXS measurements were taken with the incident beam parallel and perpendicular to the coating direction. This method yields an in-plane anisotropy between crystallites that satisfy the Bragg condition only, specifically, crystallites with edge-on π -stacks oriented parallel or perpendicular to the incidence beam. Crystallites with other in-plane orientations are not accounted for in this method, which is in contrast to the anisotropy obtained from UV-vis, whereby transition dipoles of all orientations contribute to the absorbance as discussed above. To differentiate the top interface from the bulk, we set the X-ray incident angle both above and below the critical angle of the organic layer, $\approx 0.1^\circ$, to probe the molecular packing throughout the film and near the film surface, respectively.³⁵ Above the critical angle, X-ray penetrates the entire film, whereas, below the critical angle, X-ray probes the top surface layer with approximately 5 nm

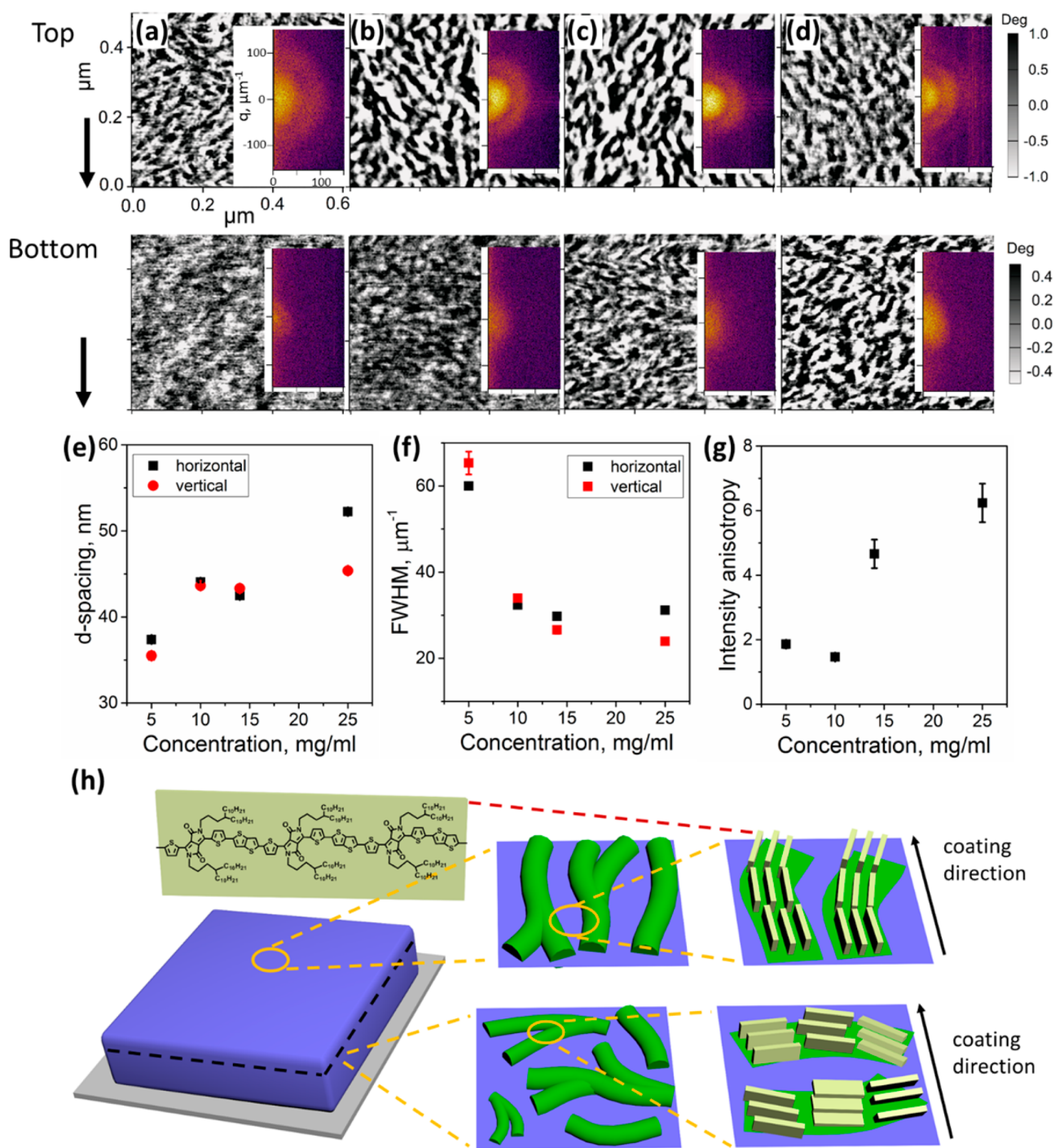


Figure 4. Tapping mode AFM phase images of DPP2T-TT thin films coated from chloroform solution at (a) 5 mg/mL, (b) 10 mg/mL, (c) 14 mg/mL, and (d) 25 mg/mL. The first row is the top interface (film–air interface) scan, and the second row is the bottom interface (film–substrate interface) scan. The inset in each phase image is the corresponding FFT image. The coating direction is denoted with the arrow on the left of each row. (e) *d*-spacing, (f) fwhm, and (g) intensity anisotropy of the horizontal and 5° offset vertical linecuts of the second-order ring from the top surface FFT. The intensity anisotropy was calculated as the ratio of horizontal peak area over the vertical peak area. (h) Schematic of film morphology and molecular stacking at the top surface vs the bulk. Green structures represent the mesoscale morphology obtained from AFM and yellow structures the molecular packing obtained from GIWAXS. Note that we assume the morphology at the bottom surface is representative of the average morphology beneath the top layer.

penetration depth, or two molecular layers.²² Surface measurements were also performed on the laminated DPP2T-TT films to study the molecular packing at the buried film–substrate interface, but no meaningful data were obtained due to the strong background scattering from the PDMS substrates used for film lamination.

Representative 2D X-ray scattering patterns from both the bulk and the surface measurements in parallel and perpendicular orientations are shown in Figure 3a. Detailed analysis on the peak area, π – π stacking distance, and peak width is summarized in Figure S6. For the bulk film, the intensity of the edge-on portion of the (010) π – π stacking peak (on the horizon) from the

perpendicular measurement is stronger than that in the parallel measurement with comparable illuminated volume for films coated from solutions of 18 mg/mL and below, indicating that the in-plane π - π stacking direction is preferentially aligned parallel to the coating direction (Figure 3b). In other words, the polymer backbone in the bulk prefers to align perpendicularly with respect to the coating direction, in agreement with the UV-vis results. However, surface measurements reveal a more intense in-plane (010) peak in the parallel direction instead, indicating that the π - π stacking is perpendicular to coating and the polymer backbone is along the coating direction at the film surface. Therefore, GIWAXS reveals an unexpected morphology outcome that the crystallites at the top surface oriented opposite to those in the bulk of the film (Figure 3c). Apart from the in-plane alignment, the out-of-plane alignment is also visible from the scattering patterns in Figure 3a. The arc-shaped scattering patterns for the (010) peak from the bulk film measurements reveal that the crystallites are misaligned in the out-of-plane orientation. However, the (010) peaks from the film surface measurements only appear near the horizon on the scattering patterns, denoting primarily edge-on crystallites at the film surface. Therefore, we can conclude that DPP2T-TT crystallites show a higher degree of alignment in both the in-plane and the out-of-plane orientations at the film surface than that in the bulk film.

To quantify the degree of in-plane alignment of the π -stacks, the ratio of the integrated peak areas (IA) for the edge-on (010) peak is calculated as $P = IA_{\text{para}}/IA_{\text{perp}}$. The edge-on portion of the (010) peak was obtained by performing a sector cut between $-88^\circ < \chi < -83^\circ$, with $\chi = -90^\circ$ representing the in-plane direction. In the bulk film, P is approximately 0.36 at the lowest concentration 5 mg/mL, and is approaching 1 with increasing concentration (Figure 3c). This trend reveals that the polymer backbone initially orients perpendicularly with the coating direction and becomes more isotropic at higher concentrations/film thicknesses. At the film surface, when the film is thin (20–30 nm), the surface alignment is consistent with the bulk; when the film becomes thicker (>70 nm), the backbone orientation significantly deviates from the bulk. The highest anisotropy $P = 4.8$ observed on the surface was obtained at the highest solution concentration 25 mg/mL, corresponding to a film thickness of 168 nm. This increasing trend in interfacial alignment with the increase of concentration/film thickness is distinct from that in the bulk. We note that similar interfacial alignment to the bulk for thin films of 20–30 nm may be a result of the difficulty in differentiating the interface from the bulk, when the interface “seen” by X-ray constitutes 20–25% of the thin film.

To complement GIWAXS measurements, we further probed mesoscale interfacial morphology at the top air–film interface and the bottom film–substrate interface using AFM. The samples for bottom interface were prepared by laminating solution coated thin films using PDMS stamps (see the Experimental Section).^{36–38} The AFM phase images in Figure 4 reveal the evolution of the interfacial morphology at the top and the bottom surfaces with respect to concentration/film thickness. At the top air–film interface, we observed short fibril-like structures with local orientational ordering, where the fibril long axis preferentially aligns along the coating direction. Combined with GIWAXS, we infer that the polymer backbone is oriented parallel to the long axis of the fibrils, and that the favorable growth kinetics along the polymer backbone conjugation direction may have resulted in the anisotropic

fibril-like morphology. Our observation is consistent with previous works on rigid donor–acceptor polymers, wherein the polymer backbone was found to align with the fiber long axis (e.g., PCDTPT,¹⁷ P(NDI2OD-T2)¹⁵). On the other hand, backbone alignment orthogonal to the fiber long axis has also been reported before, in particular for PBTTT¹⁸ and P3HT,³⁹ presumably due to their lower backbone rigidity. We further performed fast Fourier transform (FFT) to reveal the periodicity and the in-plane orientational ordering of the surface structures observed. Similar to transmission light scattering patterns, sharp and well-defined rings in the FFT image arise from the structure factor when periodic spacing emerges from the aggregated fibers with a narrow size distribution. The intensity distribution along the ring encodes information on the in-plane orientational order of the fibers. For all the top surface AFM scans, we observed rings with anisotropic intensity distributions, consistent with the well-defined fibril structures observed on the top surface. The arc on the FFT patterns exhibits higher intensity perpendicular to the coating direction, arising from the periodic spacing along the short axis of the fibrils, or equivalently, preferential orientation of the fibril long axis along the coating direction (Figure 4h). To quantify the differences observed, we performed linecuts (line width covers 30 pixels to improve signal-to-noise ratio) along the horizontal and the vertical directions (with 5° offset to avoid the vertical streak artifact) on the FFT images (Figures S7, S8). We further calculated d -spacing, full width at half-maximum (fwhm) and peak intensity anisotropy by analyzing the second order arc from the top surface FFT (Figure 4e–g). On the top surface, we observed larger d -spacing at higher concentration, which reflects increased distance between fibers and therefore increasing fiber width/diameter (Figure 4e), consistent with AFM phase images. The decreased fwhm indicates a narrower distribution and lower dispersion in fiber spacings (Figure 4f). The intensity anisotropy was calculated as the ratio of the peak area from the horizontal orientation over that from the vertical orientation. As expected, the overall intensity anisotropy increases with increasing concentration, indicating better fiber alignment at higher concentrations (Figure 4g), consistent with the inference from GIWAXS surface scans (Figure 3). On the contrary, the mesoscale morphology at the bottom film–substrate interface is significantly different compared to the top interface at the same concentration. The bottom interface does not have distinct fibril features, indicating lack of distinct periodicity, which likely arises from broad distribution of fibril size and shape. An ellipsoidal pattern extends along the coating direction in each FFT image obtained from the bottom interface scans. Judged from the pattern anisotropy (Figure S8), we infer that the long axis of the fibers weakly aligns perpendicularly to the coating direction at the bottom interface, which is orthogonal to the fiber orientation on the top interface. Because AFM can only probe the morphology at exposed interfaces, information on the mesoscale morphology in the bulk cannot be directly obtained by AFM. Nonetheless, we deduce that the morphology at the bottom interface shares similar features as that in the bulk in terms of in-plane orientation ordering. It is because the polymer backbones in the bulk and at the bottom interface are both weakly oriented orthogonal to that on the top interface, inferred from GIWAXS and AFM, respectively.

Putting the results from all morphology characterizations together, we propose a multiscale morphology model illustrated in Figure 4h, contrasting in-plane and out-of-plane alignment at the top interface vs that in the bulk. On the top interface, polymer fibrils and the backbone extend along the coating direction, with

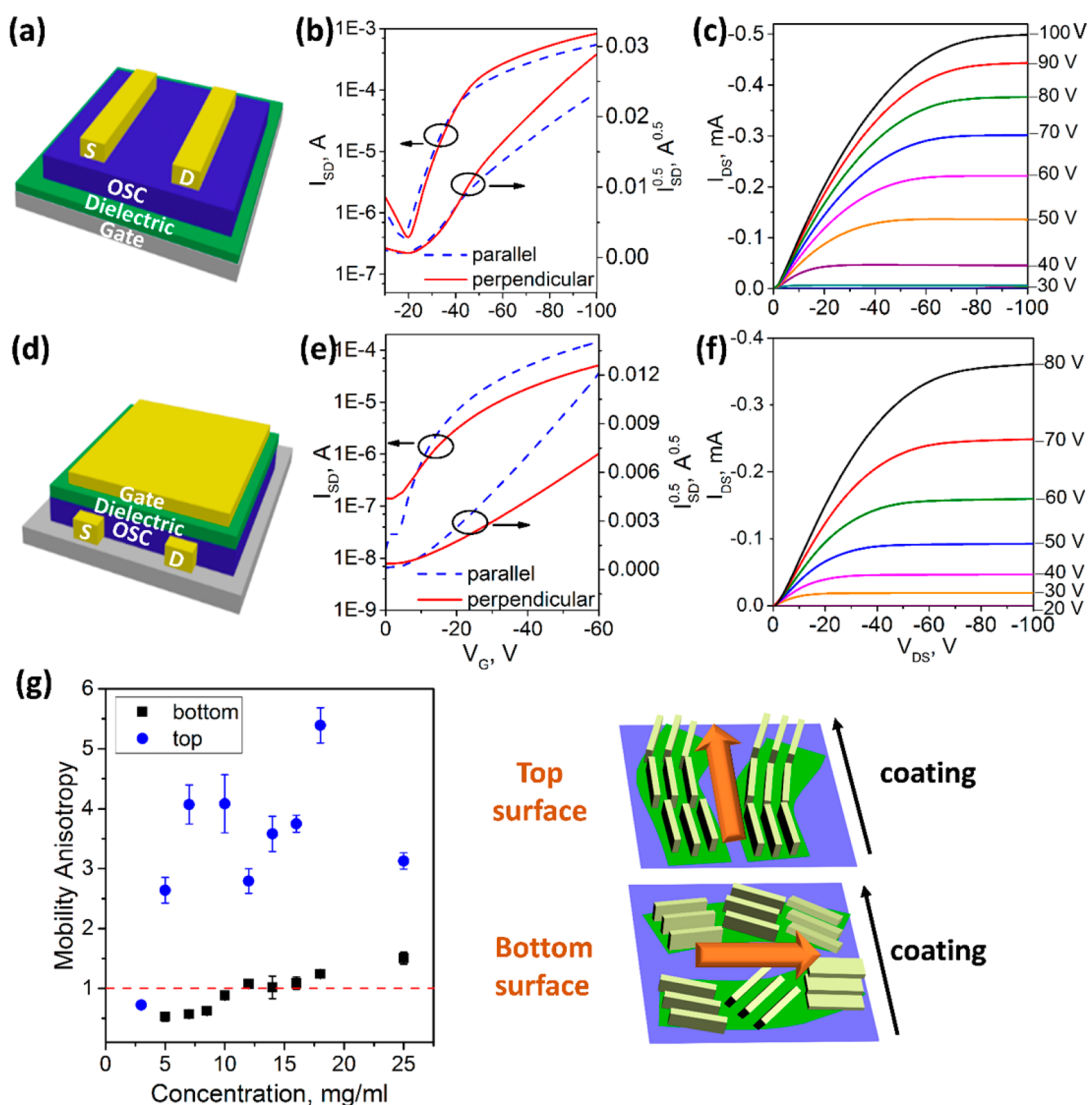


Figure 5. Comparison of FET device performance between the (a–c) BGTC configuration and (d–f) TGBC configuration. Parts (b) and (e) are representative transfer curves corresponding to films coated from 7 mg/mL solution for BGTC and 14 mg/mL for TGBC. Parts (c) and (f) are representative output curves. The measurements were performed on films coated from 7 mg/mL solution for BGTC (perpendicular) and 14 mg/mL for TGBC (parallel). The source–drain voltage V_{DS} was -100 V for the BGTC devices and -60 V for the TGBC devices. (g) Hole mobility anisotropy measured in parallel over the perpendicular direction with respect to the coating direction for both BCTG and TGBC device configurations. The anisotropy is derived from the high V_G mobilities.

the polymer backbone oriented edge-on with respect to the interface. In the bulk, the degree of alignment is significantly lower compared to that on the top interface. The long axis of the polymer fibrils and the backbone are weakly aligned transverse to the coating direction, which is opposite to that on the top interface. These distinct differences between bulk and interfacial morphology have important implications on charge transport, which we next evaluate by measuring charge carrier mobility in field-effect transistor devices.

Evaluation of Charge Transport Anisotropy. In thin film field-effect transistors (FETs), charge transport occurs within a few nanometers at the semiconductor–dielectric interface, recognized as the conducting channel.⁴⁰ By constructing both top and bottom gate FETs, we were able to quantify the charge transport properties at the top air–film interface and the bottom film–substrate interface of the solution coated thin films. We used the bottom gate top contact (BGTC) configuration (Figure 5a) and the top gate bottom contact (TGBC) configuration

(Figure 5d) to measure charge transport at the substrate–film interface and the air–film interface, respectively. The field-effect mobility μ^{sat} was determined from the transfer curves measured in the saturation regime. To determine the preferred charge transport direction and the resulting charge transport anisotropy, we fabricated devices with the channel length along both parallel and perpendicular to the coating direction. The charge transport anisotropy is defined as μ_{para}^{sat} over μ_{perp}^{sat} . The characteristic transfer and output curves comparing BGTC and TGBC devices are shown in Figure 5, and the extracted apparent mobilities from all conditions are summarized in Figure S9. For BGTC devices, we observed a persisting “kink-down” feature in the nonideal transfer characteristics (Figure 5b, Figure S10), which has been attributed to gate voltage dependent contact resistance.^{41,42} Therefore, we extracted apparent saturation mobilities from both low V_G (-20 to -50 V) and high V_G (-60 to -90 V) regions (Figure S9) and used the high V_G mobility to calculate charge transport anisotropy. Although the apparent mobilities are not

directly comparable between the BGTC and the TGBC devices given different dielectrics and different gate bias used, the charge transport anisotropy can be directly compared because it is only influenced by the interfacial morphology anisotropy as designed in our study.

The top interface exhibits significantly higher charge transport anisotropy compared to the bottom interface, which is strongly correlated with the degree of interfacial alignment observed (Figure Sg). The mobility anisotropy at the top interface is close to unity only for the thinnest film coated from 3 mg/mL solution, and is significantly higher than 1 at all other conditions when the film thickness exceeds 24 nm (above 5 mg/mL). The highest mobility anisotropy observed reaches 5.39 ± 0.05 , which is among the highest observed for DPP based polymers.^{14,19} In comparison, the mobility anisotropy on the bottom interface is close to unity for the entire concentration range studied. Mobility anisotropy > 1 on the top interface corresponds to preferred charge transport along the coating direction. Revisiting the GIWAXS results (Figure 3c), the interfacial morphology anisotropy and the charge transport anisotropy consistently point to preferred charge transport along the polymer backbone (Figure Sg).^{10,43} It can be seen that the trend of interfacial backbone alignment (Figure 3c) does not exactly match with that of the mobility anisotropy across the concentration range/film thickness studied (Figure Sg). Specifically, the mobility anisotropy is relatively insensitive to concentration change, while the degree of backbone alignment increases significantly with increasing concentration. Despite increasing backbone alignment, the grain boundary may eventually limit the charge transport given the small fibril sizes.

Similar to the top interface, the mobility anisotropy at the bottom interface shows a strong correlation with the backbone alignment in the bulk, which corroborates our hypothesis that the bottom interface has similar morphology as the bulk. At the bottom interface, charge transport is preferred perpendicular to the coating direction for thinner films/lower concentrations, and becomes almost isotropic for thicker films/higher concentrations (Figure Sg). Considering a similar trend of backbone alignment in the bulk (Figure 3c), we can conclude that the charge transport again is preferred along the polymer backbone. The mobility anisotropy approaches unity starting from 10 mg/mL, while backbone orientation becomes isotropic from 18 mg/mL. We attribute this mismatch to the onset of grain boundaries limiting charge transport before the backbone alignment is completely lost. In summary, we demonstrate that the charge transport anisotropy is substantially higher at the top interface than the bottom interface, and that the high degree of interfacial alignment induces anisotropic charge transport preferably along the DPP2T-TT polymer backbone.

DISCUSSION

The characterizations presented above indicate that the top interface exhibits a higher degree of backbone alignment at the molecular scale, larger fibrils with better in-plane orientational ordering at the mesoscale, and the resulting greater charge transport anisotropy compared to the bulk. We hypothesize that there are two key factors responsible for forming aligned nanofibers during evaporative assembly: (1) crystallization of nanofibers at the fluid–air interface due to high Peclet number and (2) alignment of nanofibers driven by the extensional character of the capillary flow at the fluid–air interface.

We first infer that the distinct interfacial morphology from that of the bulk is caused by the skin-layer formation. In other words,

the polymer crystallization starts from the top fluid–air free interface, which inhibits the evaporation of the bulk solution and delays the formation of polymer fibrils in the bulk. Compared to the bulk, longer fibrils on the free fluid–air interface experience stronger alignment effect in an extensional flow field to out-complete rotational Brownian motion. This results in higher degree of alignment on the top interface vs in the bulk. The inference of skin-layer formation is based on estimation of the dimensionless Peclet number. The Peclet number compares two competitive time scales: the rate of solvent evaporation across the liquid–air interface that establishes a vertical concentration gradient, with the rate of solute mass transport in the meniscus that diminishes the concentration gradient. We note that the estimation yielded an average Peclet number in the meniscus and did not account for its variation along the coating direction. We obtained a high Peclet number $Pe = 33$ by estimating both time scales (details in the Supporting Information). A high Peclet number indicates that the rate of solvent evaporation is significantly higher than that of solute mass transport to result in a higher polymer concentration at the top interface. Therefore, we infer that polymer crystallization ensues on the top interface when a critical concentration is reached to induce nucleation. In addition to skin-layer formation, extensional flow near the liquid–air interface may also promote polymer nucleation.

To drive in-plane alignment of as-formed polymer fibrils at the top surface, either an extensional flow or a shear flow should exist. Previous works have attributed in-plane alignment to shear flow.^{11,13,18,44} However, shear rate at the liquid–air interface is zero mandated by the boundary condition of a free surface, and therefore does not provide the driving force for alignment at the top surface. We propose that the polymer interfacial alignment is instead directed by extensional flow on the top surface, and that the difference in orientation ordering at the top surface vs in the rest of the film is caused by distinct flow characteristics on the top (extension dominant) vs in the bulk (shear dominant) of the fluid layer. The rationale is detailed below. According to previous studies, strong extensional flow exists at the top surface due to increasing solvent evaporation rate moving toward the contact line.^{45,46} Going from the free surface toward the bottom substrate, the flow type transitions from extension dominant to shear dominant, bound by the nonslip boundary condition at the bottom interface in contrast to the zero shear boundary condition at the free surface (Figure 6a).^{47,48} This flow type transition can result in distinct anisotropic particle alignment in the two different zones. For instance, Trebbin and co-workers observed, in a flow passing through an expanding channel, different orientation of fibrillary micelles in a shear dominant zone near the channel wall compared to an extension dominant zone at the channel center.⁴⁹ Simulation studies show that extensional flow is capable of aligning anisotropic particles due to differential drag along the particle.^{50,51} In the extensional flow field, the front end of a polymer fibril experiences stronger drag force than the back end. The net torque applied on the fibril is negative, rotating the fibril clockwise to align its long axis along the flow direction near the free surface (Figure 6b). In shear flows, vorticity tensor plays a dominant role instead in aligning the long axis of anisotropic particles along the vorticity tensor.^{52,53} Because the vorticity tensor is parallel to the contact line and perpendicular to the coating direction (more discussion in the Supporting Information), short polymer fibrils are aligned orthogonal to the coating direction in the bulk and near the bottom substrate (Figure 6c). The extent of orientation ordering is much lower in this case, possibly due to the relatively weak

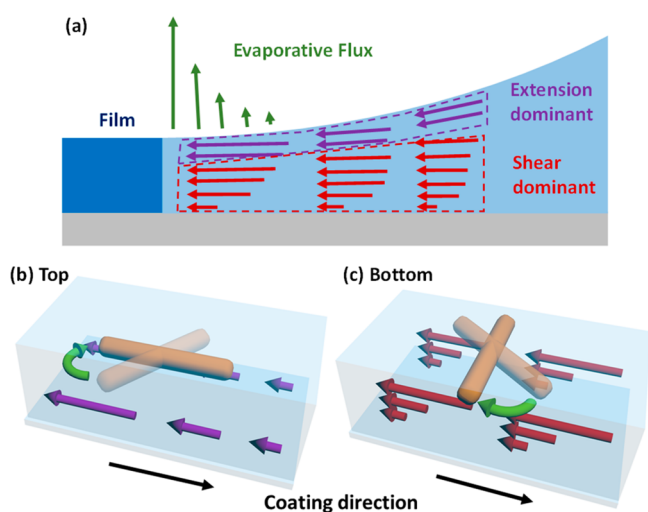


Figure 6. Illustration of alignment mechanism. (a) Schematic of the transport processes near the meniscus contact line. (b) Three-dimensional view of the in-plane alignment mechanism for an anisotropic particle in the extensional flow field. (c) Three-dimensional view of the in-plane alignment mechanism for an anisotropic particle in a shear flow field. Purple and red arrows denote the velocity vectors in the flow field, and green arrows denote the direction of rotation.

effect of shear on particle rotation.⁵⁴ The alignment mechanism proposed agrees with our morphology models built based on the GIWAXS and AFM measurements (Figure 4h). Summarizing the above discussion, we can conclude that the reasons for the better in-plane alignment near the top surface than in the bulk are the crystallization of elongated fibers at the ink–air interface, and the evaporation driven extensional flow in the top layer.

In the context of the proposed alignment mechanism during meniscus-guided solution coating, the effect of polymer concentration on alignment can also be discussed. At the top interface, the degree of alignment of polymer fibrils increases with increasing solution concentration (Figure 3). It is because polymer fibrils crystallize earlier at higher starting concentrations under the same evaporation rate (Figure S1), leaving more time for fiber growth and reorientation under extensional flow. Thus, the in-plane alignment increases monotonically with solution concentration. On the other hand, the in-plane orientation of the polymer fibrils becomes more isotropic in the bulk of the film when the concentration increases. At higher starting concentration, the liquid film trapped underneath the skin layer is thicker given earlier onset of crystallization. Since the shear flow is imposed by the nonslip boundary condition at the substrate, the thicker liquid layer weakens the effect of shear-induced alignment outcompeted by the Brownian motion to decrease the degree of alignment in the bulk of the solidified film.

CONCLUSION

In summary, we fabricated DPP2T-TT thin films and OFET devices using meniscus-guided coating and observed backbone alignment and charge transport anisotropy at the air–film interface distinct from that in the bulk of the film. Revealed by GIWAXS, AFM, and polarized UV–vis, the polymer fibrils near the top interface exhibit a significantly higher degree of alignment than the bulk under most conditions studied. Specifically, well-defined polymer fibrils were observed at the top interface, with the long axis and the polymer backbone aligned along the coating direction. In contrast, the bulk fibrils were significantly smaller,

either weakly aligned transverse to coating or close to isotropic. Correspondingly, the charge transport at the air–film interface showed markedly higher mobility anisotropy while the charge transport at the film–substrate interface remains weakly anisotropic or almost isotropic. Interestingly, the charge transport prefers to occur along the polymer backbone direction, even in the cases when the fibrils were only weakly aligned. We hypothesize that the in-plane alignment of the DPP2T-TT fibers is driven by the extensional flow at the ink–air interface near the contact line. Nanofibers form near the interface where a concentration gradient occurs due to the high evaporation rate, and are aligned by the extensional flow. This alignment mechanism can be a reference for molecular or deposition process design to achieve high degree of alignment in conjugated polymer thin films for both kinetic studies and charge transport characterizations.

EXPERIMENTAL SECTION

Substrate Treatment. Octyldecyltrichlorosilane (Acros 95%) was used to perform substrate treatment to reduce charge traps for device fabrication. The ODTs was stored in the refrigerator at 4 °C and was removed from the refrigerator before sample preparation. In the glovebox, 100 μ L of ODTs was transferred into a 1 mL syringe and 50 mL of anhydrous trichloroethylene was transferred to a 250 mL bottle. A 4 in. Si wafer with a 300 nm thick SiO₂ layer was plasma treated for 6 min and placed in a glass Petri dish. The ODTs was injected into the trichloroethylene, and the mixture was poured into the Petri dish. The Petri dish was covered and sealed with aluminum foil and parafilm. The reaction was left at room temperature for 20 min. After reaction, the wafer was removed from the solution and was rinsed with toluene. The dry wafer was placed on a hot plate at 120 °C for 2 min to induce 2D crystallization of ODTs before removal and storage.

Synthesis of DPP-TT. The conjugated polymer DPP2T-TT ($M_n = 20\,000$ g/mol, $M_w = 104\,000$ g/mol, PDI = 5.2) was synthesized following a previous published procedure.⁵⁵ 3,6-Bis(5-bromothiophen-2-yl)-2,5-bis(4-decyltetradecyl)pyrrolo[3,4-*c*]pyrrole-1,4(2*H*,5*H*)-dione (300.0 mg, 265.2 mmol) and 2,5-bis(trimethylstannyl)thieno[3,2-*b*]thiophene (123.5 mg, 265.2 mmol) were dissolved in 20 mL of toluene in a 35 mL microwave reaction vessel. The solution was purged with nitrogen for 15 min, before tris(*o*-tolyl)phosphine (3 mg) and tris(dibenzylideneacetone)dipalladium(0) (6 mg) were added. The vessel was sealed with a snap cap and quickly transferred to a CEM Discover Microwave Reactor. Reaction conditions were listed as follows: Power cycling mode; Power, 300 W; Power cycles, 100; Temperature, 120–150 °C; Heating, 120 s; Cooling, 30 s; Pressure, 150 psi; Stirring, high. After the reaction was complete, the polymer was collected by precipitation into methanol. The product was dissolved in 50 mL of chloroform, and palladium was removed with 30 mg of *N,N*-diethylphenylazothioformamide at 50 °C for 30 min. The solution was precipitated into methanol, and the solid was dried under 60 °C over high vacuum.

Film Preparation. Polymer DPP2T-TT was dissolved in chloroform (Macron ACS grade) at 25 mg/mL and stirred overnight in a nitrogen environment to ensure dissolution. DPP2T-TT thin films were deposited onto substrates by a meniscus-guided coating method using an ODTs-treated Si blade.^{26,27} The meniscus-guided coating setup involves a stationary substrate and a moving blade, with ink solution sandwiched in-between. The blade was tilted by 7°, with the blade edge set 100 μ m above the substrate surface for the film deposition process. The speed of the blade was 0.5 mm/s for all samples, and the substrate temperature was fixed at 25 °C. The solution was diluted to the designated concentration during film deposition. For microscopy, AFM, and GIWAXS, DPP2T-TT films were prepared on ODTs-treated SiO₂-Si substrates, and for UV–vis spectroscopy, films were prepared on ODTs-treated glass slides.

UV–vis Spectroscopy. Solid-state transmission UV–vis spectroscopy measurements were performed on the Agilent Cary 60 UV–vis spectrometer. DPP2T-TT thin films coated on ODTs-treated glass

substrates were mounted on the solid sample holder with a vertical polarizer sheet. The scans were taken from 400 to 1000 nm.

Atomic Force Microscopy Measurements. AFM measurements were performed on the Asylum Cypher AFM with Tap300Al-G tapping mode AFM tips. The top air–film interface scans were performed on the films as prepared on substrates. The film–substrate interface scans were performed on laminated films on PDMS. The PDMS stamp for lamination was prepared by mixing Momentive RIV615 silicone potting compound and cross-linking agent RTV615 by the volume ratio of 10:1. The mixture was sufficiently mixed and poured into a clean plastic Petri dish until the liquid layer thickness is ~ 5 mm. The Petri dish with polymer was placed in a house vacuum oven at 50 °C for 2 h. Low curing temperature was chosen to ensure stickiness of the PDMS surface to facilitate film transfer. After curing, the PDMS stamp was cut and placed onto a newly coated polymer film. The PDMS stamp was gently pressed on the film and quickly lifted from one corner to transfer the film from the substrate. AFM scans were performed on the exposed bottom interface of film on PDMS. Linecuts with a 30 pixel line width along the horizontal direction and with a 5° offset along the vertical direction were performed on the top surface FFT images. Raw data were smoothed to reduce the noise from the pixelated FFT images. Peak deconvolution was performed to separate the first-order peak in the center and the second-order arc. The second-order peak was fitted with a Gaussian function to obtain the peak position, peak area, and the full width half-maximum (fwhm).

Small-Angle Neutron Scattering. Small-angle neutron scattering (SANS) experiments were performed at the National Institute of Standards and Technology Center for Neutron Research (NIST CNR) in Gaithersburg, MD. SANS measurements were performed on the NGB 30m beamline at three detector positions to obtain the scattering intensity, $I(q)$, over a wide q -range ($0.004 < q$ (Å⁻¹) < 0.4).⁵⁶ DPPTT was dissolved in *d*-chloroform ($D > 99.8\%$, Cambridge Isotopes) by mixing for 6 h prior to loading in a 1 mm path length demountable cells with quartz windows. The total scattering was normalized to the incident beam flux, corrected for background scattering (e.g., empty cell and solvent), and 2D profiles were then converted to 1D profiles using standard methods.⁵⁷ Smear model fitting was performed using DANSE SASView software.⁵⁸

Grazing Incidence Wide-Angle X-ray Scattering. GIWAXS measurements were performed at beamline 8-ID-E of Advanced Photon Source at the Argonne National Laboratory.⁵⁹ Data were collected with an incident beam energy at 7.35 keV on a two-dimensional detector (Pilatus 1M) at two different positions and the images combined to eliminate most of the inactive pixels using the GIXSGUI package written for Matlab.⁶⁰ GIXSGUI was also used to apply corrections for detector nonuniformity, beam polarization, and detector sensitivity, and to reshape the two-dimensional data into the representation q_z vs q_r ($= \sqrt{q_x^2 + q_y^2}$). Experiments were carried out in a helium chamber. The incident angle was set at 0.2° for bulk measurements and 0.08° for surface measurements. For calculating the π – π stacking anisotropy, P , we extracted the intensity of the edge-on portion of the π – π stacking peak from both parallel and perpendicular scans, by performing a sector cut of $-88^\circ < \chi < -83^\circ$ from the raw data image. Peak deconvolution was performed to separate the π – π stacking peak from the amorphous peak, the background scattering, and the peak from crystalline ODTs. The π – π stacking peak was fitted with a Gaussian function to obtain the peak position, peak area, and the full width half-maximum (fwhm).

Device Fabrication and Characterizations. The bottom gate top contact configuration was used to measure charge transport at the bottom interface. For BGTC device fabrication, DPP2T-TT/chloroform solution was coated on ODTs treated 300 nm SiO₂-Si substrates, and gold source–drain electrodes were evaporated on top of the DPP2T-TT thin film. For TGBC device fabrication, DPP2T-TT/chloroform solution was coated on substrates with evaporated gold source–drain electrodes. On the DPP2T-TT film, we next spin-coated a layer of CYTOP, a trademarked fluorinated polymer dielectric with low trap density, and another gold layer was evaporated on top as the gate electrode. Specifically, the source and drain electrodes were 35 nm thick Au deposited by thermal evaporation. The channel length and width

were 70 and 4500 μm , respectively. The top gate bottom contact configuration was used to measure charge transport at the top interface. The source and drain electrodes had the same dimensions as in the BGTC configuration deposited by the same method. A 447 ± 3 nm CYTOP layer was spin-coated at 2000 rpm for 1 min on top of the electrodes and polymer thin film serving as a dielectric. Immediately after spin-coating, the CYTOP film was annealed at 100 °C for 30 min on a hot plate. A 35 nm gold layer was thermally evaporated on the CYTOP layer as a gate. A Keysight B1500A analyzer was used for all FET device measurements in a glovebox under a nitrogen environment. The BGTC devices were measured as deposited, and the TGBC devices were measured after annealing for CYTOP cross-linking. Gate bias between 0 and -100 V with a drain voltage of -100 V was applied for BGTC device measurements and between 0 and -60 V with a drain voltage of -60 V was applied for TGBC device measurements to avoid device burning. The apparent mobility in the saturation regime was calculated using the equation $\mu_{\text{sat}} = \frac{2L}{WC_i} \left(\frac{d\sqrt{I_{\text{SD}}}}{dV_G} \right)^2$. The capacitance for

the 300 nm SiO₂ layer and the CYTOP layer is estimated with $C = \frac{\epsilon\epsilon_0}{d_0}$, where ϵ is the relative permittivity of the insulator (3.9 for SiO₂ and 2.1 for CYTOP), ϵ_0 is the air permittivity, and d_0 is the thickness. The capacitance of CYTOP was calculated to be 4.2 nF/cm². With consideration of the influence of the ODTs layer,⁶¹ the capacitance of SiO₂ used for calculation is 11 nF/cm².

■ ASSOCIATED CONTENT

📄 Supporting Information

The Supporting Information is available free of charge on the ACS Publications website at DOI: 10.1021/acsami.7b08133.

Details on the film thickness analysis, UV–vis spectroscopy peak shift and peak height data, GIWAXS π – π stacking peak position, peak area and fwhm data, BGTC and TGBC device mobilities, sample mobility versus gate voltage plots, and Peclet number calculations (PDF)

■ AUTHOR INFORMATION

Corresponding Author

*E-mail: yingdiao@illinois.edu.

ORCID

Jianguo Mei: 0000-0002-5743-2715

Ying Diao: 0000-0002-8984-0051

Notes

The authors declare no competing financial interest.

■ ACKNOWLEDGMENTS

This research was financially supported by the startup funds of University of Illinois. Y.D. and G.Q. gratefully acknowledge partial support by the National Science Foundation, Division of Materials Research, under grant number #1641854. J.M. acknowledges the financial support from the Office of Naval Research Young Investigator Program (ONR YIP), award number N00014-16-1-2551. This research used resources of the Advanced Photon Source, a U.S. Department of Energy (DOE), Office of Science User Facility, operated for the DOE Office of Science by Argonne National Laboratory under Contract No. DE-AC02-06CH11357. Part of this research was performed in the Frederick Seitz Materials Research Laboratory Central Facilities, University of Illinois. Part of this research is based upon work supported by the U.S. Department of Energy, Office of Science, Office of Basic Energy Science, under award number DE-SC0005153. We acknowledge the support of the National Institute of Standards and Technology, U.S. Department of Commerce, in providing the neutron research facilities

used in this work. This work utilized facilities supported in part by the National Science Foundation under Agreement No. DMR-1508249. This work benefitted from SasView software, originally developed by the DANSE project under NSF award DMR-0520547. The authors thank Dr. F. Spano at the Temple University for helpful discussions on UV-vis spectroscopy.

REFERENCES

- (1) Himmelberger, S.; Salleo, A. Engineering Semiconducting Polymers for Efficient Charge Transport. *MRS Commun.* **2015**, *5*, 383–395.
- (2) Noriega, R.; Rivnay, J.; Vandewal, K.; Koch, F. P.; Stingelin, N.; Smith, P.; Toney, M. F.; Salleo, A. A General Relationship between Disorder, Aggregation and Charge Transport in Conjugated Polymers. *Nat. Mater.* **2013**, *12*, 1038–1044.
- (3) Venkateshvaran, D.; Nikolka, M.; Sadhanala, A.; Lemaur, V.; Zelazny, M.; Kepa, M.; Hurhangee, M.; Kronemeijer, A. J.; Pecunia, V.; Nasrallah, I.; Romanov, I.; Broch, K.; McCulloch, I.; Emin, D.; Olivier, Y.; Cornil, J.; Beljonne, D.; Sirringhaus, H. Approaching Disorder-Free Transport in High-Mobility Conjugated Polymers. *Nature* **2014**, *515*, 384–388.
- (4) Zhang, X.; Bronstein, H.; Kronemeijer, A. J.; Smith, J.; Kim, Y.; Kline, R. J.; Richter, L. J.; Anthopoulos, T. D.; Sirringhaus, H.; Song, K.; Heeney, M.; Zhang, W.; McCulloch, I.; DeLongchamp, D. M. Molecular Origin of High Field-Effect Mobility in an Indacenodithiophene–Benzothiadiazole Copolymer. *Nat. Commun.* **2013**, *4*, 2238.
- (5) Pingel, P.; Zen, A.; Abellón, R. D.; Grozema, F. C.; Siebbeles, L. D. A.; Neher, D. Temperature-Resolved Local and Macroscopic Charge Carrier Transport in Thin P3ht Layers. *Adv. Funct. Mater.* **2010**, *20*, 2286–2295.
- (6) Bolsée, J.-C.; Oosterbaan, W. D.; Lutsen, L.; Vanderzande, D.; Manca, J. The Importance of Bridging Points for Charge Transport in Webs of Conjugated Polymer Nanofibers. *Adv. Funct. Mater.* **2013**, *23*, 862–869.
- (7) Noriega, R.; Salleo, A.; Spakowitz, A. J. Chain Conformations Dictate Multiscale Charge Transport Phenomena in Disordered Semiconducting Polymers. *Proc. Natl. Acad. Sci. U. S. A.* **2013**, *110*, 16315–16320.
- (8) Jimison, L. H.; Toney, M. F.; McCulloch, I.; Heeney, M.; Salleo, A. Charge-Transport Anisotropy Due to Grain Boundaries in Directionally Crystallized Thin Films of Regioregular Poly(3-Hexylthiophene). *Adv. Mater.* **2009**, *21*, 1568–1572.
- (9) Rivnay, J.; Jimison, L. H.; Northrup, J. E.; Toney, M. F.; Noriega, R.; Lu, S.; Marks, T. J.; Facchetti, A.; Salleo, A. Large Modulation of Carrier Transport by Grain-Boundary Molecular Packing and Microstructure in Organic Thin Films. *Nat. Mater.* **2009**, *8*, 952–958.
- (10) Tseng, H. R.; Phan, H.; Luo, C.; Wang, M.; Perez, L. A.; Patel, S. N.; Ying, L.; Kramer, E. J.; Nguyen, T. Q.; Bazan, G. C.; Heeger, A. J. High-Mobility Field-Effect Transistors Fabricated with Macroscopic Aligned Semiconducting Polymers. *Adv. Mater.* **2014**, *26*, 2993–2998.
- (11) Kim, B. G.; Jeong, E. J.; Chung, J. W.; Seo, S.; Koo, B.; Kim, J. A Molecular Design Principle of Lyotropic Liquid-Crystalline Conjugated Polymers with Directed Alignment Capability for Plastic Electronics. *Nat. Mater.* **2013**, *12*, 659–664.
- (12) Soeda, J.; Matsui, H.; Okamoto, T.; Osaka, I.; Takimiya, K.; Takeya, J. Highly Oriented Polymer Semiconductor Films Compressed at the Surface of Ionic Liquids for High-Performance Polymeric Organic Field-Effect Transistors. *Adv. Mater.* **2014**, *26*, 6430–6435.
- (13) Bucella, S. G.; Luzio, A.; Gann, E.; Thomsen, L.; McNeill, C. R.; Pace, G.; Perinot, A.; Chen, Z.; Facchetti, A.; Caironi, M. Macroscopic and High-Throughput Printing of Aligned Nanostructured Polymer Semiconductors for MHz Large-Area Electronics. *Nat. Commun.* **2015**, *6*, 8394.
- (14) Schott, S.; Gann, E.; Thomsen, L.; Jung, S. H.; Lee, J. K.; McNeill, C. R.; Sirringhaus, H. Charge-Transport Anisotropy in a Uniaxially Aligned Diketopyrrolopyrrole-Based Copolymer. *Adv. Mater.* **2015**, *27*, 7356–7364.
- (15) Biniek, L.; Leclerc, N.; Heiser, T.; Bechara, R.; Brinkmann, M. Large Scale Alignment and Charge Transport Anisotropy of Pbtth Films Oriented by High Temperature Rubbing. *Macromolecules* **2013**, *46*, 4014–4023.
- (16) Kyaw, A. K. K.; Lay, L. S.; Peng, G. W.; Changyun, J.; Jie, Z. A Nanogroove-Guided Slot-Die Coating Technique for Highly Ordered Polymer Films and High-Mobility Transistors. *Chem. Commun.* **2016**, *52*, 358–361.
- (17) Tseng, H. R.; Ying, L.; Hsu, B. B.; Perez, L. A.; Takacs, C. J.; Bazan, G. C.; Heeger, A. J. High Mobility Field Effect Transistors Based on Macroscopically Oriented Regioregular Copolymers. *Nano Lett.* **2012**, *12*, 6353–6357.
- (18) DeLongchamp, D. M.; Kline, R. J.; Jung, Y.; Germack, D. S.; Lin, E. K.; Moad, A. J.; Richter, L. J.; Toney, M. F.; Heeney, M.; McCulloch, I. Controlling the Orientation of Terraced Nanoscale “Ribbons” of a Poly(Thiophene) Semiconductor. *ACS Nano* **2009**, *3*, 780–787.
- (19) Shaw, L.; Hayoz, P.; Diao, Y.; Reinspach, J. A.; To, J. W. F.; Toney, M. F.; Weitz, R. T.; Bao, Z. Direct Uniaxial Alignment of a Donor-Acceptor Semiconducting Polymer Using Single-Step Solution Shearing. *ACS Appl. Mater. Interfaces* **2016**, *8*, 9285–9296.
- (20) Chang, J.; Lin, Z.; Li, J.; Lim, S. L.; Wang, F.; Li, G.; Zhang, J.; Wu, J. Enhanced Polymer Thin Film Transistor Performance by Carefully Controlling the Solution Self-Assembly and Film Alignment with Slot Die Coating. *Adv. Electron. Mater.* **2015**, *1*, 1500036.
- (21) Joseph Kline, R.; McGehee, M. D.; Toney, M. F. Highly Oriented Crystals at the Buried Interface in Polythiophene Thin-Film Transistors. *Nat. Mater.* **2006**, *5*, 222–228.
- (22) Schuettfort, T.; Thomsen, L.; McNeill, C. R. Observation of a Distinct Surface Molecular Orientation in Films of a High Mobility Conjugated Polymer. *J. Am. Chem. Soc.* **2013**, *135*, 1092–1101.
- (23) Himmelberger, S.; Dacuña, J.; Rivnay, J.; Jimison, L. H.; McCarthy-Ward, T.; Heeney, M.; McCulloch, I.; Toney, M. F.; Salleo, A. Effects of Confinement on Microstructure and Charge Transport in High Performance Semicrystalline Polymer Semiconductors. *Adv. Funct. Mater.* **2013**, *23*, 2091–2098.
- (24) Schuettfort, T.; Watts, B.; Thomsen, L.; Lee, M.; Sirringhaus, H.; McNeill, C. R. Microstructure of Polycrystalline Pbtth Films: Domain Mapping and Structure Formation. *ACS Nano* **2012**, *6*, 1849–1864.
- (25) Patel, S. N.; Su, G. M.; Luo, C.; Wang, M.; Perez, L. A.; Fischer, D. A.; Prendergast, D.; Bazan, G. C.; Heeger, A. J.; Chabinc, M. L.; Kramer, E. J. Nexafs Spectroscopy Reveals the Molecular Orientation in Blade-Coated Pyridal[2,1,3]Thiadiazole-Containing Conjugated Polymer Thin Films. *Macromolecules* **2015**, *48*, 6606–6616.
- (26) Giri, G.; Verploegen, E.; Mannsfeld, S. C.; Atahan-Evrenk, S.; Kim, D. H.; Lee, S. Y.; Becerril, H. A.; Aspuru-Guzik, A.; Toney, M. F.; Bao, Z. Tuning Charge Transport in Solution-Sheared Organic Semiconductors Using Lattice Strain. *Nature* **2011**, *480*, 504–508.
- (27) Becerril, H. A.; Roberts, M. E.; Liu, Z.; Locklin, J.; Bao, Z. High-Performance Organic Thin-Film Transistors through Solution-Sheared Deposition of Small-Molecule Organic Semiconductors. *Adv. Mater.* **2008**, *20*, 2588–2594.
- (28) Deegan, R. D.; Bakajin, O.; Dupont, T. F.; Huber, G.; Nagel, S. R.; Witten, T. A. Capillary Flow as the Cause of Ring Stains from Dried Liquid Drops. *Nature* **1997**, *389*, 827–829.
- (29) Köhler, A.; dos Santos, D. A.; Beljonne, D.; Shuai, Z.; Brédas, J.-L.; Holmes, A. B.; Kraus, A.; Müllen, K.; Friend, R. H. Charge Separation in Localized and Delocalized Electronic States in Polymeric Semiconductors. *Nature* **1998**, *392*, 903–906.
- (30) Comoretto, D.; Dellepiane, G.; Marabelli, F.; Cornil, J.; dos Santos, D. A.; Bredas, J. L.; Moses, D. Optical Constants of Highly Stretch-Oriented Poly(P-Phenylene-Vinylene): A Joint Experimental and Theoretical Study. *Phys. Rev. B: Condens. Matter Mater. Phys.* **2000**, *62*, 10173–10184.
- (31) Gather, M. C.; Bradley, D. D. C. An Improved Optical Method for Determining the Order Parameter in Thin Oriented Molecular Films and Demonstration of a Highly Axial Dipole Moment for the Lowest Energy $\Pi-\Pi^*$ Optical Transition in Poly(9,9'-Diocetylfluorene-Co-Bithiophene). *Adv. Funct. Mater.* **2007**, *17*, 479–485.

- (32) Vezie, M. S.; Few, S.; Meager, I.; Pieridou, G.; Dorling, B.; Ashraf, R. S.; Goni, A. R.; Bronstein, H.; McCulloch, I.; Hayes, S. C.; Campoy-Quiles, M.; Nelson, J. Exploring the Origin of High Optical Absorption in Conjugated Polymers. *Nat. Mater.* **2016**, *15*, 746–753.
- (33) O'Connor, B. T.; Reid, O. G.; Zhang, X.; Kline, R. J.; Richter, L. J.; Gundlach, D. J.; DeLongchamp, D. M.; Toney, M. F.; Kopidakis, N.; Rumbles, G. Morphological Origin of Charge Transport Anisotropy in Aligned Polythiophene Thin Films. *Adv. Funct. Mater.* **2014**, *24*, 3422–3431.
- (34) O'Connor, B.; Kline, R. J.; Conrad, B. R.; Richter, L. J.; Gundlach, D.; Toney, M. F.; DeLongchamp, D. M. Anisotropic Structure and Charge Transport in Highly Strain-Aligned Regioregular Poly(3-Hexylthiophene). *Adv. Funct. Mater.* **2011**, *21*, 3697–3705.
- (35) Rivnay, J.; Mannsfeld, S. C.; Miller, C. E.; Salleo, A.; Toney, M. F. Quantitative Determination of Organic Semiconductor Microstructure from the Molecular to Device Scale. *Chem. Rev.* **2012**, *112*, 5488–5519.
- (36) DeLongchamp, D. M.; Kline, R. J.; Fischer, D. A.; Richter, L. J.; Toney, M. F. Molecular Characterization of Organic Electronic Films. *Adv. Mater.* **2011**, *23*, 319–337.
- (37) Kim, J. B.; Lee, S.; Toney, M. F.; Chen, Z.; Facchetti, A.; Kim, Y. S.; Loo, Y.-L. Reversible Soft-Contact Lamination and Delamination for Non-Invasive Fabrication and Characterization of Bulk-Heterojunction and Bilayer Organic Solar Cells. *Chem. Mater.* **2010**, *22*, 4931–4938.
- (38) Chabinyo, M. L.; Salleo, A.; Wu, Y.; Liu, P.; Ong, B. S.; Heeney, M.; McCulloch, I. Lamination Method for the Study of Interfaces in Polymeric Thin Film Transistors. *J. Am. Chem. Soc.* **2004**, *126*, 13928–13929.
- (39) Wang, G.; Persson, N.; Chu, P.-H.; Kleinhenz, N.; Fu, B.; Chang, M.; Deb, N.; Mao, Y.; Wang, H.; Grover, M. A.; Reichmanis, E. Microfluidic Crystal Engineering of Π -Conjugated Polymers. *ACS Nano* **2015**, *9*, 8220–8230.
- (40) Coropceanu, V.; Cornil, J.; da Silva Filho, D. A.; Olivier, Y.; Silbey, R.; Bredas, J. L. Charge Transport in Organic Semiconductors. *Chem. Rev.* **2007**, *107*, 926–952.
- (41) Bittle, E. G.; Basham, J. I.; Jackson, T. N.; Jurchescu, O. D.; Gundlach, D. J. Mobility Overestimation Due to Gated Contacts in Organic Field-Effect Transistors. *Nat. Commun.* **2016**, *7*, 10908.
- (42) Uemura, T.; Rolin, C.; Ke, T.-H.; Fesenko, P.; Genoe, J.; Heremans, P.; Takeya, J. On the Extraction of Charge Carrier Mobility in High-Mobility Organic Transistors. *Adv. Mater.* **2016**, *28*, 151–155.
- (43) Lee, M. J.; Gupta, D.; Zhao, N.; Heeney, M.; McCulloch, I.; Sirringhaus, H. Anisotropy of Charge Transport in a Uniaxially Aligned and Chain-Extended, High-Mobility, Conjugated Polymer Semiconductor. *Adv. Funct. Mater.* **2011**, *21*, 932–940.
- (44) Lee, W. H.; Cho, J. H.; Cho, K. Control of Mesoscale and Nanoscale Ordering of Organic Semiconductors at the Gate Dielectric/Semiconductor Interface for Organic Transistors. *J. Mater. Chem.* **2010**, *20*, 2549–2561.
- (45) Doumenc, F.; Guerrier, B. Drying of a Solution in a Meniscus: A Model Coupling the Liquid and the Gas Phases. *Langmuir* **2010**, *26*, 13959–13967.
- (46) Hsueh, C.; Doumenc, F.; Guerrier, B. Numerical Simulation of Complex Fluid Drying in a Hele-Shaw Cell. *Eur. Phys. J.: Spec. Top.* **2013**, *219*, 51–57.
- (47) Doumenc, F.; Salmon, J. B.; Guerrier, B. Modeling Flow Coating of Colloidal Dispersions in the Evaporative Regime: Prediction of Deposit Thickness. *Langmuir* **2016**, *32*, 13657–13668.
- (48) Romero, O. J.; Suszynski, W. J.; Scriven, L. E.; Carvalho, M. S. Low-Flow Limit in Slot Coating of Dilute Solutions of High Molecular Weight Polymer. *J. Non-Newtonian Fluid Mech.* **2004**, *118*, 137–156.
- (49) Trebbin, M.; Steinhäuser, D.; Perlich, J.; Buffet, A.; Roth, S. V.; Zimmermann, W.; Thiele, J.; Förster, S. Anisotropic Particles Align Perpendicular to the Flow Direction in Narrow Microchannels. *Proc. Natl. Acad. Sci. U. S. A.* **2013**, *110*, 6706–6711.
- (50) Parsa, S.; Guasto, J. S.; Kishore, M.; Ouellette, N. T.; Gollub, J. P.; Voth, G. A. Rotation and Alignment of Rods in Two-Dimensional Chaotic Flow. *Phys. Fluids* **2011**, *23*, 043302.
- (51) Qazi, S. J.; Rennie, A. R.; Tucker, I.; Penfold, J.; Grillo, I. Alignment of Dispersions of Plate-Like Colloidal Particles of Ni(OH)₂ Induced by Elongational Flow. *J. Phys. Chem. B* **2011**, *115*, 3271–3280.
- (52) Franceschini, A.; Filippidi, E.; Guazzelli, E.; Pine, D. J. Transverse Alignment of Fibers in a Periodically Sheared Suspension: An Absorbing Phase Transition with a Slowly Varying Control Parameter. *Phys. Rev. Lett.* **2011**, *107*, 250603.
- (53) Xie, D.; Lista, M.; Qiao, G. G.; Dunstan, D. E. Shear Induced Alignment of Low Aspect Ratio Gold Nanorods in Newtonian Fluids. *J. Phys. Chem. Lett.* **2015**, *6*, 3815–3820.
- (54) Lambert, G. M.; Baird, D. G. Evaluating Rigid and Semiflexible Fiber Orientation Evolution Models in Simple Flows. *J. Manuf. Sci. Eng.* **2017**, *139*, 031012.
- (55) Chen, Z.; Lee, M. J.; Shahid Ashraf, R.; Gu, Y.; Albert-Seifried, S.; Meedom Nielsen, M.; Schroeder, B.; Anthopoulos, T. D.; Heeney, M.; McCulloch, I.; Sirringhaus, H. High-Performance Ambipolar Diketopyrrolopyrrole-Thieno[3,2-B]Thiophene Copolymer Field-Effect Transistors with Balanced Hole and Electron Mobilities. *Adv. Mater.* **2012**, *24*, 647–652.
- (56) Glinka, C. J.; Barker, J. G.; Hammouda, B.; Krueger, S.; Moyer, J. J.; Orts, W. J. The 30 M Small-Angle Neutron Scattering Instruments at the National Institute of Standards and Technology. *J. Appl. Crystallogr.* **1998**, *31*, 430–445.
- (57) Kline, S. Reduction and Analysis of SANS and USANS Data Using Igor Pro. *J. Appl. Crystallogr.* **2006**, *39*, 895–900.
- (58) Alina, G.; Bakker, J.; Bouwman, W.; Butler, P.; Campbell, K.; Cho, J.-H.; Hernandez, R. C.; Doucet, M.; Gonzalez, M.; Heenan, R.; Jackson, A.; Kienzle, P.; King, S.; Kline, S.; Kryzwon, J.; Mannicke, D.; Markvardsen, A.; Nielsen, T.; Parker, P.; Richter, T.; Whitley, R.; Zhou, J. *SasView for Small Angle Scattering Analysis*. <http://www.sasview.org/> (Accessed April 2016).
- (59) Jiang, Z.; Li, X.; Strzalka, J.; Sprung, M.; Sun, T.; Sandy, A. R.; Narayanan, S.; Lee, D. R.; Wang, J. The Dedicated High-Resolution Grazing-Incidence X-Ray Scattering Beamline 8-ID-E at the Advanced Photon Source. *J. Synchrotron Radiat.* **2012**, *19*, 627–636.
- (60) Jiang, Z. Gixsgui: A Matlab Toolbox for Grazing-Incidence X-Ray Scattering Data Visualization and Reduction, and Indexing of Buried Three-Dimensional Periodic Nanostructured Films. *J. Appl. Crystallogr.* **2015**, *48*, 917–926.
- (61) Oh, J. H.; Lee, H. W.; Mannsfeld, S.; Stoltenberg, R. M.; Jung, E.; Jin, Y. W.; Kim, J. M.; Yoo, J.-B.; Bao, Z. Solution-Processed, High-Performance N-Channel Organic Microwave Transistors. *Proc. Natl. Acad. Sci. U. S. A.* **2009**, *106*, 6065–6070.